Nigerian Journal of Applied Physics (NJAP)
ISSN Print: 3115-5871
ISSN Online: 3115-588X
DOI: https://doi.org/10.62292/njap-v2i4-2026-124
Volume 2(4), November 2026

# Band Engineering and Miniband Formation in InPBi/AlGaAs Quantum Dot Superlattices

***[1]Ikedichukwu O. Onyekwere, [2]Chijioke I. Oriaku, [2]Lebe A. Nnanna and [2]Chinkata Joseph Uwaoma.**

[1]Physics Department, Claretian University of Nigeria, Maryland Nekede, Nigeria
[2]Physics Department, Michael Okpara University of Agriculture Umudike, Nigeria

*Corresponding Author's Email: ikedichukwuonyekwere@gmail.com

**Keywords:**
Quantum dot superlattices,
Band alignment,
Strain balancing,
Miniband,
InPBi.

Submitted: 03/11/2026

Accepted: 16/11/2026

Published:24/11/2026

**ABSTRACT**

Quantum dot superlattices (QDSLs) for intermediate-band solar cells require quantum dots that provide carrier confinement, self-assembly, and sufficient strain tolerance for multilayer growth. This study develops a theoretical framework for $InP_{1-x}Bi_x/\ Al_{0.40}Ga_{0.60}As$ QDSLs that combines composition-dependent band parameters, strain-induced valence-band coupling, strain compensation, and BenDaniel-Duke Kronig–Penney modelling to identify design conditions for intermediate-band formation. This integrated treatment provides a specific extension beyond isolated band-alignment or quantum-dot confinement calculations by simultaneously relating Bi composition, dot geometry, spacer thickness, strain compensation, and miniband formation. The model predicts type-I alignment with conduction-band offsets of 0.40-0.42 eV and heavy-hole offsets of 0.25-0.40 eV. Strain coupling to the split-off band is predicted to stabilize the light-hole state with predominantly in-plane character. GaP sheets of 0.55-0.78 nm per period are predicted to compensate the approximately 4% compressive strain. The calculated intermediate-band widths are 3-18 meV, with intermediate-band gaps of 0.19-0.25 eV and 1.24-1.51 eV. Design maps identify dot heights near 4 nm and spacer thicknesses of approximately 2–3 nm or less as favourable for miniband formation. These results are theoretical predictions and remain sensitive to alloy disorder, local strain fluctuations, interface roughness, and Bi segregation or partitioning, which are not explicitly resolved by the present model. Experimental measurements of in-dot strain and InPBi/AlGaAs band offsets, together with atomistic or multiscale calculations, are therefore required to test the predictions.

## INTRODUCTION

An intermediate band solar cell (IBSC) adds a narrow band of states inside the gap of a host semiconductor, so that two photons with energies below the gap can together promote an electron from the valence band (VB) to the conduction band (CB) through the intermediate band (IB), while the voltage remains limited by the host gap (Luque and Marti,1997; 2010; Luque *et al*.,2012). Its detailed-balance efficiency limit of 63% under maximum concentration exceeds the Shockley-Queisser limit of a single gap (Luque and Marti, 2010; Shockley and Queisser, 1961) and the concept has been reviewed repeatedly as experimental devices have matured (Okada *et al*., 2015; Ramiro and Marti, 2021; Almosni *et al*., 2018; Neupane *et al*., 2026).

Quantum dot superlattices (QDSLs) are the most developed IBSC absorbers (Marti *et al*., 2001;2006; Antolin *et al*., 2010; Ramiro *et al*., 2020). In a vertical stack of self assembled dots, the confined electron ground state of each dot couples to its neighbours by tunnelling and broadens into a miniband, which plays the role of the IB (Lazarenkova and Balandin, 2001; Tomic and Harrison, 2008, Tomic, 2010; Popescu *et al*., 2008). Dots grown by the Stranski-Krastanov (SK) mode on a mismatched substrate align vertically through their strain fields, which is what makes such stacks superlattices rather than random ensembles (Leonard et *al*., 1993; Xie *et al*., 1995; Solomon *et al*., 1996; Tersoff *et al*., 1996). Before any optical or device question can be addressed, three structural questions must therefore be answered: whether both carriers are confined in the dots, whether the mismatch drives SK growth, and

whether the accumulated strain can be balanced over many periods. Each answer depends on the band offsets and lattice constants of the chosen materials (Vurgaftman *et al*., 2001; Van de Walle, 1989; Bimberg *et al*., 1999).

Dilute bismides are attractive dot materials because bismuth acts mainly on the valence band. In $InP_{1-x}Bi_x$, contactless electroreflectance gives a gap reduction of 83 meV per percent Bi and a much smaller change of, $E_0 + \Delta_{so}$ consistent with valence band anticrossing, while absorption gives a similar reduction of 91 meV per percent Bi (Kopaczek *et al*.,2014; Wu *et al*., 2016; Alberi *et al*., 2007; Polak *et al*., 2015). InPBi layers with up to about 3% Bi have been grown by molecular beam epitaxy, (Wang *et al*., 2014; Gu *et al*., 2014; Pan *et al*., 2016; Zhang *et al*., 2017; Wang *et al*., 2017; Akahane *et al*., 2022) and their deep level photoluminescence has been traced to Bi clusters and $P_{In}$ antisites (Wu *et al*., 2016; Chen *et al*., 2017). The only dedicated modeling of InPBi dots placed them in an $Al_{0.42}Ga_{0.58}As$ matrix on GaAs and found a type-I alignment (Zhang *et al*., 2019; Zhang *et al*., 2018).

The choice of host is therefore the first design decision. On an InP substrate the mismatch of InPBi is only about 0.3%, far too small to drive SK island formation, so a strongly mismatched substrate such as GaAs is needed (Vurgaftman *et al*., 2001; Wu *et al*., 2016). This paper establishes the band parameters, band offsets, strain balance and minibands of InPBi dots in $Al_{0.40}Ga_{0.60}As$ on GaAs (001), with GaP strain-compensation sheets in each spacer (Ekins-Daukes *et al*., 2002; Hubbard *et al*., 2008; Sugaya *et al*., 2012). Future work will use these results to compute optical transition strengths, polarization-resolved absorption and device feasibility.

Section 2 sets out the material parameters, the strain and band-offset model, the strain balance condition and the Kronig-Penney (KP) model. Section 3 selects the host, quantifies the alignment and strain balance, and presents the minibands and design maps of three representative designs. Section 4 summarises the design rules

## MATERIALS AND METHODS

### Theoretical methods

All constituent parameters are taken from the compilation of Vurgaftman, Meyer and Ram- Mohan (Vurgaftman *et al*., 2001) unless stated otherwise, and are listed with their sources in Table 1. The Bi-induced band shifts are derived from the contactless-electroreflectance slopes of Kopaczek *et al*. 2014. If the split-off band is unaffected by Bi, as valence-band anticrossing predicts, (Alberi *et al*., 2007; Broderick *et al*., 2012), the measured $dE_0/dx = -83meV/\%$ and $d(E_0 + \Delta_{so})/dx = -13meV$ imply a CB shift of -13 meV/% and a VB rise of +70 meV/%. The same data imply that the spin-orbit splitting grows from the InP value of 0.108 eV by 70 meV/%, $\Delta_{so}(x) = 0.108 + 0.070x\ eV$ with $x$ in percent, which enters the light-hole edge below. The lattice constant of InPBi follows Vegard's law with the extrapolated InBi value of 6.52 $^0$A (Shalindar *et al*., 2016; Wu *et al*., 2016). Effective masses along the growth axis and in the plane follow from the Luttinger parameters, (Vurgaftman *et al*., 2001; Lutiinger *et al*., 1956) with $m_{hh,z} = (\gamma_1 - 2\gamma_2)^{-1}$, $m_{lh,z} = (\gamma_1 + 2\gamma_2)^{-1}$, $m_{hh,\|} = (\gamma_1 + \gamma_2)^{-1}$ and $m_{lh,\|} = (\gamma_1 - \gamma_2)^{-1}$ in units of $m_0$. Host parameters are interpolated linearly in the Al fraction. Three quantities are model choices rather than material constants: the strain retention factor ζ, the dot radius R and the areal dot density $\sigma_{QD}$. Their values are typical of SK dots and are justified in Sec. 2.2 (Bimberg *et al*., 1999; Grundmann *et al*., 1995; Vullum *et al*., 2017).

**Table 1: Input parameters (300 K) and their sources. Dot: InPBi; host AlGaAs; VBO is the valence band offset on the common scale of Ref.(Vurgaftman *et al*., 2001).**

| Quantity | Symbol | Value |
|---|---|---|
| Lattice constant | $a_{GaAs}, a_{InP}, a_{GaP}$ | 5.6533, 5.8688, 5.4505 $\dot{A}$ |
| InBi lattice cont. | $a_{InBi}$ | 6.52 $\dot{A}$ |
| InP gap, VBO | $E_g, E_v$ | 1.344, -0.94 eV |
| Bi shift of VB and CB | $dE_v/dx\ , dE_c/dx$ | +70, -13 meV/% |
| InP elastic constants | $C_{11}, C_{12}$ | 101.1, 56.1 GPa |
| GaP elastic constant | $C_{11}, C_{12}$ | 140.5, 62.0 GPa |
| InP deformation potentials | $a_c, a_v, b$ | -6.0, -0.6, -2.0 eV |
| InPLuttinger parameters | $\gamma_1, \gamma_2$ | 5.08, 1.60 |
| InP electron mass | $m_{e,}$ | $0.0795\ m_0$ |
| Host gap (Γ), VBO | $E_g^{host}, E_v^{host}$ | 1.923, -1.012 eV |
| Host electron mass | $m_{e,b}$ | $0.100\ m_0$ |
| Luttinger parameters | $\gamma_1, \gamma_2$ | 5.69, 1.56 |
| Derived masses (dot/host) | $m_{hhz}; m_{lh,z}$ | 0.532/0.390; 0.121/0.113 |
| In-plane masses (dot) | $m_{hh,\|}; m_{lh,\|}$ | 0.150; 0.287 |
| In-dot strain retention | Z | 0.60 |

| | | |
|---|---|---|
| Dot radius, areal density | $R, \sigma_{QD}$ | 10 nm, $5 \times 10^{10} cm^{-2}$ |
| Wetting layer | $t_{WL}$ | 1.5 ML |

Pseudomorphic growth on GaAs imposes the biaxial strain $\varepsilon_{xx}^{(0)} = (a_{GaAs} - a_{dot})/a_{dot}$ and, through the Poisson response, $\varepsilon_{zz}^{(0)} = -2(C_{12}/C_{11})\varepsilon_{xx}^{(0)}$. Inside an SK dot part of this strain relaxes elastically through the free facets (Grundmann *et al*., 1995; Stier *et al*., 1999). Strain mapping of InAs/GaAs dots by electron microscopy shows in-dot strains well below the pseudomorphic values, (Vullum *et al*., 2017) and we represent this relaxation by a single retention factor, $\varepsilon_{ij} = \zeta\varepsilon_{ij}^{(0)}$ with $\zeta$ = 0.6, with $\varepsilon_H = 2\varepsilon_{xx} + \varepsilon_{zz}$, model-solid theory (Van de Walle, 1989) gives the strained band edges

$$E_c = E_v^{InP} + E_g^{InP} + \frac{dE_c}{dx}x + a_c\varepsilon_H \quad (1)$$

In the valence band, biaxial strain shifts the in-plane orbitals $X, Y$ by $e_{xy} = a_v\varepsilon_H + b(\varepsilon_{xx} - \varepsilon_{zz})$ and the axial orbital $Z$ by $e_z = a_v\varepsilon_H - 2b(\varepsilon_{xx} - \varepsilon_{zz})$. The heavy hole (HH) is a pure $X, Y$ state, but the light hole (LH) is coupled by strain to the split-off band. Because $\Delta_{so}$ of InP (0.108 eV) is comparable with the shear term, this coupling cannot be neglected. The $m_J = 1/2$ block of the six-band strain and spin-orbit Hamiltonian, in the basis $\{|1,\downarrow\rangle, |0,\uparrow\rangle\}$ of orbital angular momentum and spin, has diagonal elements $e_A = e_{xy} - 2\Delta_{so}/3$ and $e_B = e_z - \Delta_{so}/3$ and off-diagonal element $\sqrt{2\Delta_{so}/3}$. Its upper root is the light-hole edge. The valence edges are therefore (Chuang, 1991; Chuang, 2009)

$$E_{hh,} = E_v^{InP} + \frac{dE_v}{dx}x + a_c\varepsilon_H \pm b(\varepsilon_{xx} - \varepsilon_{zz}), \quad (2)$$

$$E_{lh} = E_v^{InP} + \frac{dE_v}{dx}x + \frac{1}{2}(e_A + e_B) + \sqrt{\frac{1}{4}\left(e_A - e_B\right)^2 + \frac{2}{9}\Delta_{so}^2} \quad (3)$$

For $\Delta_{so} \to \infty$ the second line reduces to the familiar four-band result $a_v\varepsilon_H - b(\varepsilon_{xx} - \varepsilon_{zz})$. Because $b < 0$ and $\varepsilon_{xx} < \varepsilon_{zz}$ under compression, the HH edge lies above the LH edge. The eigenvector of the upper root fixes the orbital composition of the light hole: a weight $w_Z$ on the axial orbital and $w_X = w_Y = (1 - w_Z)/2$ on each in-plane orbital. These weights set its optical selection rules and its masses,

$$m_{lh,z}^{-1} = (1 - w_Z)(\gamma_1 - 2\gamma_2) + w_Z(\gamma_1 + 4\gamma_2) \quad (4)$$

and

$$m_{lh,\parallel}^{-1} = w_X(\gamma_1 + 4) + (w_X + w_Z)(\gamma_1 - 2) \quad (5)$$

which reduce to the Luttinger values for the decoupled weights $w_Z = 2/3$ and $w_X = 1/6$. The confining offsets are $\Delta E_c = E_c^{host} - E_c$ and $\Delta E_{v,hh(lh)} = E_{hh(lh)} - E_v^{host}$, and a positive value means the carrier is confined in the dot.

Each period contains a compressively strained InPBi layer of equivalent thickness $t_{QD}$, made up of a 1.5 ML wetting layer plus the dot volume per unit area $\pi R^2\sigma_{QD}h$, and a GaP sheet under tension. The zero-stress condition of Ekins-Daukes *et al*. 2002 gives the GaP thickness that makes the average in-plane stress of a period vanish:

$$t_{GaP} = t_{QD}\frac{A_{QD}|\varepsilon_{QD}|a_{GaP}}{A_{GaP}\varepsilon_{GaP}a_{QD}}, \qquad A = C_{11} + C_{12} - \frac{2C_{12}^2}{C_{11}} \quad (6)$$

The GaP sheet itself must remain coherent. Its Mathews-Blakselee critical thickness on GaAs, for $60^0$ dislocations with Burgers vector $b_d = a_{GaAs}/\sqrt{2}$, follows from (Matthews and Blakeslee, 1974)

$$h_c = \frac{b_d(1-v/4)}{2\pi f(1+v)}\left[In\left(\frac{h_c}{b_d}\right) + 1\right], \qquad v = \frac{C_{12}}{C_{11}+C_{12}}, \quad (7)$$

which is solved by fixed-point iteration.

The envelope Hamiltonian of carrier $\alpha \in \{e, hh, lh\}$ is separated into an axial and a lateral part (Harrison and Valavanis, 2016; Bastard, 1981). Along the growth axis z the BenDaniel-Duke operator (BenDaniel and Duke,1966)

$$\hat{H}_\alpha^{(z)} = -\frac{\hbar^2}{2}\frac{d}{dz}\frac{1}{m_\alpha(z)}\frac{d}{dz} + V_\alpha(z), \quad (8)$$

$$V_\alpha(z) = \begin{cases} 0, & |z| < h/2 \\ \Delta E_{\alpha,} & h/2 < |z| < a/2 \end{cases} \quad (9)$$

acts on a periodic square well of period $a = h + d$, where h is the dot height and d the spacer thickness. Hole energies are measured downward from the dot valence edge. With $k_w = \sqrt{2m_wE/\hbar}$ in the dot and $k = \sqrt{2m_b(\Delta E - E)/\hbar}$ in the spacer, continuity of $\psi$ and $m - 1\psi^{\prime}$ together with the Bloch condition give the Kronig-Penney dispersion (Bastard, 1981; Kronig and Penny, 1931)

$$\cos(k_z\, a) = \cos(k_w h)\cosh(kd) + \frac{1}{2}(\xi - \xi^{-1})\sin(k_w h)\sinh(kd), \quad \xi = \frac{km_w}{k_w m_b}, \quad (10)$$

for $E < \Delta E$. Above the barrier, $k \to ik_b$ turns the hyperbolic functions into trigonometric ones. Equation (10) corrects the sign of the second term used in the earlier version of this model. Its roots give the band edges at $k_z = 0$ and $k_z = \pi/a$. The full dispersion and the Bloch envelopes are obtained by diagonalising the same periodic problem in a basis of 61 plane waves,

$$H_{GG^{\prime}}(k_z) = \frac{\hbar^2}{2}(k_z + G)[m^{-1}]_{G-G^{\prime}}\left(k_z + G^{\prime}\right) + V_{G-G^{\prime}}, \quad (11)$$

$$|f|_G = f_b\delta_{G0} + (f_w - f_b)\frac{h}{a}\frac{\sin(Gh/2)}{Gh/2} \quad (12)$$

with $G = 2\pi n/a$.

Laterally, each dot is a cylinder of radius, $R$ and depth, $\Delta E_\alpha$. Iits ground state satisfies $q^{J_1}(qR)K_0(pR) = pK_1(pR)J_0(qR)$ with $q^2 + p^2 = 2m_{\alpha,\parallel}\Delta E_\alpha/\hbar^2$, and the lateral energy is $E_{\alpha,\text{⍰}} = \hbar^2q^2/2m_{\alpha,\parallel}$(Harrison and

Valavanis, 2016). The IB is the lowest electron miniband, $E_{IB}(k_z) = E_c + E_{e,\square} + E_{e1}(k_z)$,
(13)
and the top hole level is

$$E_{hh1}(k_z) = E_{hh} - E_{hh,\square} - E_{hh1}^{(z)}(k_z) \quad (14)$$

When dots are tall enough, a second electron level $e2$ is bound below the host CB edge. Carriers in $e2$ exchange rapidly with the CB, so we take the effective CB edge as $E_C^* = min(E_c^{host}, E_{e2}^{bottom})$. The two sub-gaps and the effective gap are

$$E_L = E_C^* - E_{IB}^{top},\ E_H = E_{IB}^{bottom} - E_{hh1}^{top},\ E_g^* = E_C^* - E_{hh1}^{top} = E_L + E_H + W_{IB}, \quad (15)$$

Where $W_{IB}$ is the IB width. Holes in the dense HH ladder are taken to share the VB quasi- Fermi level (Popescu *et al*., 2008; Kronig and Penny, 1931). The penalty that a bound $e2$ level places on $E_L$ is the confined-ladder limitation known from InAs/GaAs dots (Luque *et al*., 2012; Tomic *et al*., 2011; Aspnes, 1976).

## RESULTS AND DISCUSSION

Figure 1 and Table 2 compare five hosts for an $InP_{0.97}Bi_{0.025}$ dot. On InP substrates the mismatch is only 0.28%, too small to drive SK islanding, which in InAs/GaAs requires about 7% and in practice proceeds readily above about 2% (Leonard *et al*, 1993; Bimberg *et al*., 1999). InP confines holes but leaves a 24 meV electron offset, too shallow for an IB. $In_{0.52}Ga_{0.48}As$ confines electrons but gives a hole offset of only 28 meV.

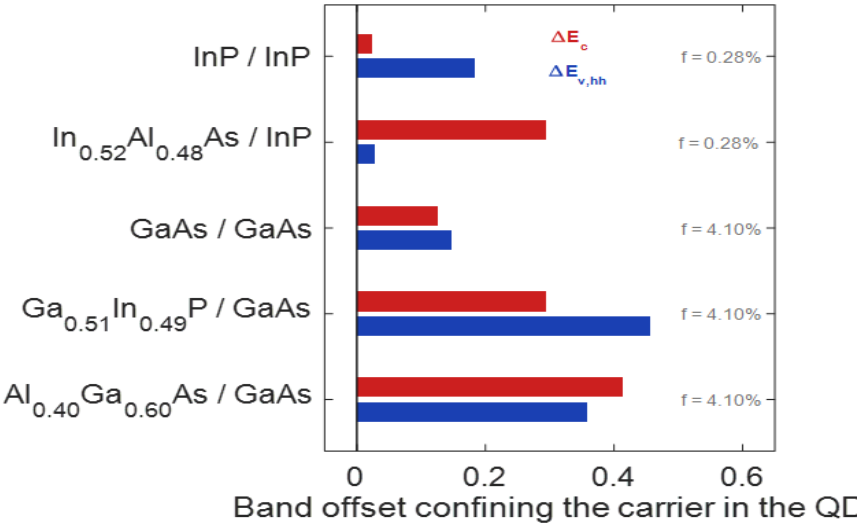



Figure 1: Confining band offsets of $InP_{0.975}Bi_{0.025}$ dots in five candidate hosts (300 K, ζ = 0.6). Positive values confine the carrier in the dot. The mismatch $f$ between dot and substrate is given on the right.

On GaAs substrates the mismatch rises to 4.10%, close to the SK regime of InAs/GaAs. GaAs itself gives shallow offsets of 0.13 and 0.15 eV. $Ga_{0.51}In_{0.49}P$ and $Al_{0.40}Ga_{0.60}As$ both give a type-I alignment with gaps near 1.9 eV. We adopt $Al_{0.40}Ga_{0.60}As$ because it gives the largest electron offset (0.413 eV), which sets the depth of the IB, and because it is the matrix used for the only previous InPBi-dot modeling (Zhang *et al*., 2019). At y = 0.40 the host gap is still direct, with the X minimum about 50 meV higher (Vurgaftman *et al*., 2001; Aspnes,1976) $Ga_{0.51}In_{0.49}P$ remains a viable alternative with a deeper hole well (Pryor and Pistol, 2005; Kim *et al*., 2002; Hatami *et al*., 2003).

**Table 2: Host materials for $InP_{0.97}Bi_{0.025}$ dots (computed). $f$ is the dot/substrate mismatch.**

| Host/substrate | $f$(%) | $E_g^{host}$ $(eV)$ | $\Delta E_c$ $(eV)$ | $\Delta E_{v,hh}$ $(eV)$ |
|---|---|---|---|---|
| InP/InP | 0.28 | 1.344 | +0.024 | +0.183 |
| $In_{0.52}Al_{0.48}As/InP$ | 0.28 | 1.460 | +0.294 | +0.028 |
| GaAs / GaAs | 4.10 | 1.424 | +0.126 | +0.147 |
| $Ga_{0.51}In_{0.49}P/GaAs$ | 4.10 | 1.900 | +0.294 | +0.456 |
| $Al_{0.40}Ga_{0.60}As/GaAs$ | 4.10 | 1.923 | +0.413 | +0.359 |

Three designs span the parameter space. Design A has short dots ($h = 3\,nm$), thick spacers ($d = 6\,nm$) and 1% Bi. Design B has $h = d = 4\,nm$ and 2% Bi. Design C has tall dots $h = 5\,nm$, thin spacers $d = 2.5\,nm$ and

3% Bi. The radius of 10 nm and the heights of 3-5 nm are typical of SK dots, (Zhang *et al*., 2019; Bimberg *et al*., 1999) and the Bi range matches demonstrated InPBi growth (Kopaczek *et al*., 2014; Wu *et al*., 2016; Wang *et al*., 2014).

Figure 2 shows the band-edge profiles along $z$ with the confined levels, and Table 3 lists the strains and offsets. The in-dot strain is close to $\varepsilon_{xx} = -2.3\%$ and $\varepsilon_{zz} = +2.6$ in all designs, and the hydrostatic strain of about -2.1% raises the CB edge through $a_c\varepsilon_H$. The electron offset barely changes with Bi (0.399 to 0.418 eV), whereas the HH offset rises from 0.250 to 0.396 eV, at nearly the 70 meV/% rate of the VB shift. The dot gap correspondingly falls from 1.274 to 1.109 eV. All three designs are type-I for both HH and LH.

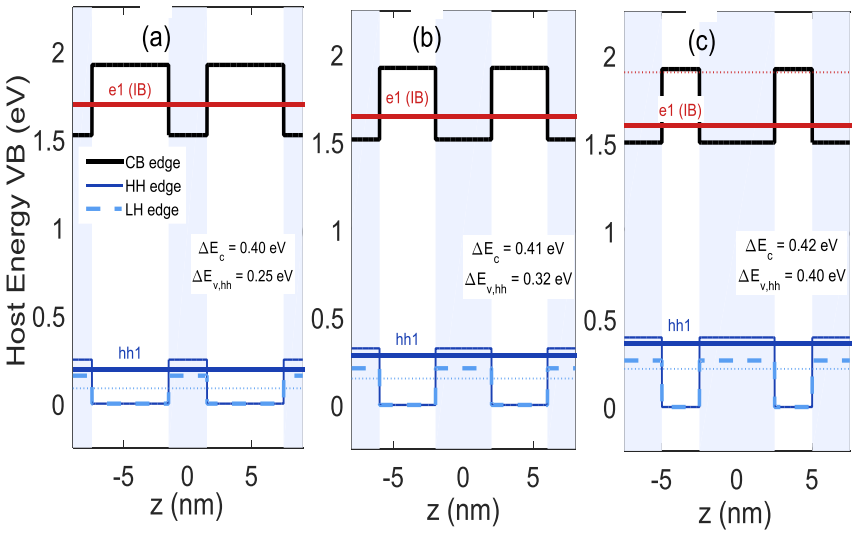



Figure 2: Band-edge profiles along the growth axis for Designs A, B and C over two periods, measured from the host VB edge. Shaded regions are InPBi dot layers. Solid black: CB edge. Blue: HH edge. Dashed light blue: LH edge. Red: IB ($e1$) level, with the bound $e2$ level dotted in Design C. Blue horizontal lines: hh1 and lh1 levels.

**Table 3: Strain and band alignment of the three designs (computed; host gap 1.923 eV).**

| Design | $x$(%) | $\varepsilon_{xx}$ | $\varepsilon_{zz}$ | $\varepsilon_H$ | $\Delta E_c$ ($eV$) | $\Delta E_{v,hh}$ ($eV$) | $\Delta E_{v.lh}$ ($eV$) | $E_g^{dot}$ ($eV$) |
|---|---|---|---|---|---|---|---|---|
| A | 1.0 | -0.023 | 0.025 | -0.020 | 0.399 | 0.250 | 0.058 | 1.274 |
| B | 2.0 | -0.023 | 0.026 | -0.020 | 0.408 | 0.323 | 0.126 | 1.192 |
| C | 3.0 | -0.024 | 0.027 | -0.021 | 0.418 | 0.396 | 0.194 | 1.109 |

Figure 3 follows the offsets and gaps over $0 \le x \le 4\%$ . The electron offset rises slowly from 0.399 to 0.418 eV, while the HH offset rises from 0.250 to 0.396 eV and overtakes the electron offset near $x = 3.3\%$. The six-band LH offset is positive at every Bi content. It is 0.115 eV at $x = 0$ and rises to 0.32 eV at 4%. The four-band model, which neglects the coupling to the split-off band, would place the LH edge 9 meV below the host VB edge at $x = 0$ and bind it only above $x = 0.14\%$ (dotted line). The coupling raises the LH edge by 0.12 eV at $x = 0$ and by 0.07 eV at 3%. It weakens with Bi because $\Delta_{so}$ grows. The HH-LH edge splitting therefore grows with Bi, from 0.06 to 0.15 eV, instead of staying near 0.19 eV. The coupling also changes the character of the light hole (Table 4). Its axial weight $w_Z$ is only 0.04 at $x = 0$ and rises to 0.10, 0.16 and 0.23 at 1, 2 and 3% Bi, compared with 2/3 for a decoupled light hole. The light hole is thus mainly an in-plane state, with a heavy axial mass of 0.25-0.44 $m_0$. Bismuth controls this character through $\Delta_{so}$, which makes the Bi content the polarization lever of the VB→IB transition. The strained dot gap falls from 1.36 to 1.03 eV. The effective gaps $E_g^*$ of the confined designs lie 0.34-0.46 eV above the dot gap because of confinement, and well below the host gap.

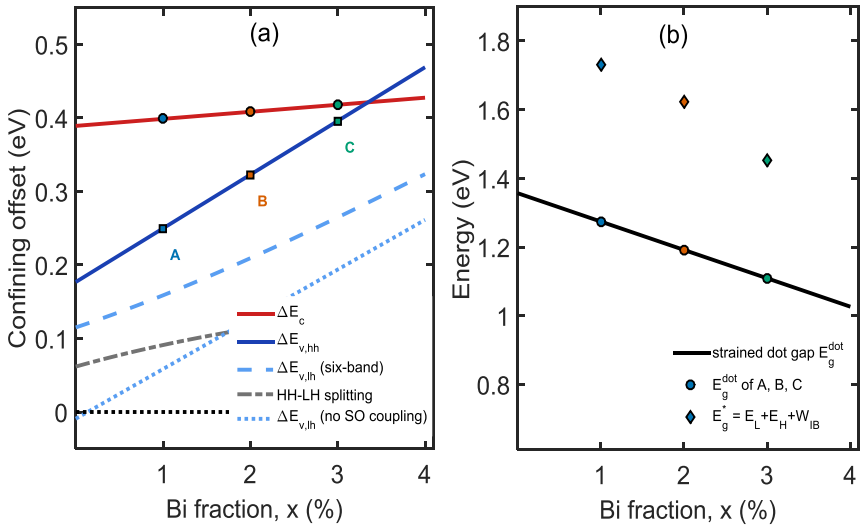



Figure 3: (a) Confining offsets $\Delta E_c$, $\Delta E_{v,hh}$ and $\Delta E_{v,lh}$, and the HH-LH edge splitting, versus Bi fraction. Symbols mark Designs A, B and C. (b) Strained dot gap versus Bi fraction, with the dot gaps and effective gaps $E_g^*$ of the three designs.

**Table 4: Six-band light-hole character versus Bi fraction (computed, in-dot strain with $\zeta = 0.6$). 'Rise' is the upward shift of the LH edge caused by the coupling to the split-off band; $w_X$ and $w_Z$ are the in-plane and axial orbital weights.**

| $x$(%) | $\Delta_{so}$ ($eV$) | Rise (eV) | $\Delta E_{v,lh}$ ($eV$) | $w_X$ | $w_Z$ | $m_{lh,z}$ ($m_0$) | $m_{lh,\parallel}$ ($m_0$) |
|---|---|---|---|---|---|---|---|
| 0 | 0.108 | 0.124 | 0.115 | 0.481 | 0.039 | 0.444 | 0.154 |
| 1 | 0.178 | 0.100 | 0.159 | 0.451 | 0.098 | 0.355 | 0.161 |
| 2 | 0.248 | 0.083 | 0.209 | 0.418 | 0.164 | 0.290 | 0.170 |
| 3 | 0.318 | 0.071 | 0.265 | 0.387 | 0.225 | 0.247 | 0.179 |

Figure 4 shows the in-dot strain components and the zero-stress GaP thickness, and Table 5 lists the values for the designs. The equivalent InPBi thickness per period grows from 0.91 to 1.23 nm with dot height, and the GaP thickness required by Eq. (6) grows from 0.55 to 0.78 nm. These sheets are only 14-20% of the Matthews-Blakeslee critical thickness of GaP on GaAs (3.99 nm for a mismatch of 3.72%), so each sheet stays coherent. Because every period is stress-free on average, the strain does not accumulate with the number of periods. Stacks of more than 100 layers are therefore possible in principle, as demonstrated for strain-balanced InAs/GaAs dot stacks (Hubbard *et al*., 2008; Sugaya *et al*., 2012; Kim *et al*., 2002; Bailey *et al*., 2011). The GaP sheet should be placed a few nanometres above each dot layer so that it does not disturb the vertical strain coupling that aligns the dots (Xie *et al*., 1995; Tersoff *et al*., 1996).

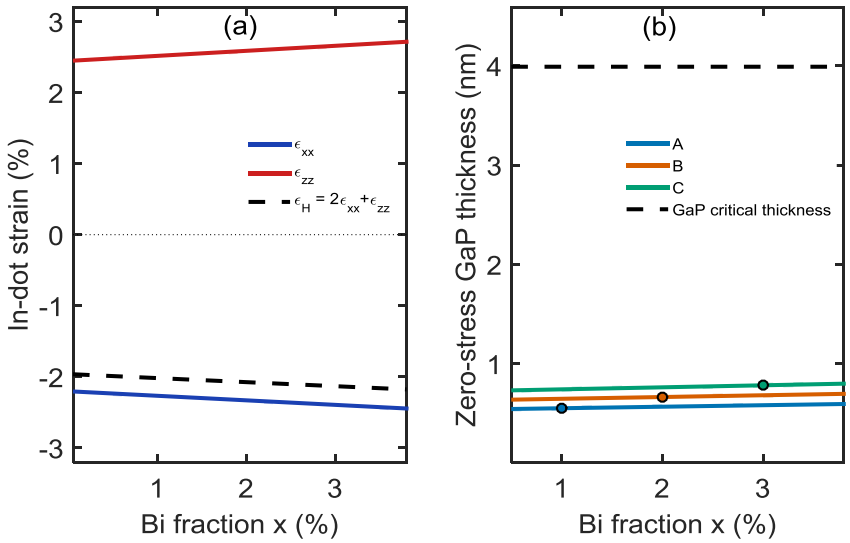



Figure 4: (a) In-dot strain components versus Bi fraction (ζ = 0.6). (b) Zero-stress GaP thickness per period Eq. (6) for dot heights of 3, 4 and 5 nm, compared with the Matthews-Blakeslee critical thickness of GaP on GaAs Eq. (7). Symbols mark Designs A, B and C.

**Table 5: Strain balance with GaP sheets (computed). $t_{QD}$ is the equivalent InPBi thickness per period (wetting layer plus dots).**

| Design | $f(\%)$ | $t_{QD}\,(nm)$ | $t_{GaP}(nm)$ | $h_c(nm)$ | $t_{GaP}/h_c$ |
|---|---|---|---|---|---|
| A | 3.93 | 0.912 | 0.552 | 3.99 | 0.138 |
| B | 4.04 | 0.069 | 0.665 | 3.99 | 0.167 |
| C | 4.16 | 1.227 | 0.783 | 3.99 | 0.196 |

Figure 5 shows the minibands of the three designs and Table 6 lists their parameters. The plane wave band edges agree with the analytic roots of Eq. (10) to within 0.05 meV in every design, which validates both solutions. The IB centre lies 1.699, 1.649 and 1.613 eV above the host VB edge and falls with dot height as confinement weakens. The IB width grows from 2.95 meV in Design A to 7.63 meV in B and 17.78 meV in C, following the thinner spacers. Design A has a single bound electron miniband, and its e2 level lies 43 meV above the host CB edge. In Design B, e2 is bound 20 meV below the host edge, less than $K_{BT}$. In Design C it is bound 109 meV below the edge and pins the effective CB edge. The lateral electron energy is 22.5 meV in all designs, set by the 10 nm radius.

The heavy holes form dot localised levels rather than a miniband. The hh1 width stays below 0.2 meV even for the 2.5 nm spacer of Design C, because the HH mass along $z$ is six times the electron mass. This supports treating the HH ladder as part of the VB reservoir (Popescu *et al*., 2008; Kronig and Penny, 1931).

**Table 6: Miniband parameters. Energies are measured from the host VB edge. $n_b$ and $n_h$ are the numbers of bound electron and HH $z-$minibands, $l_e$ is the electron decay length in the spacer $P_{KP} = m_b\,\Delta E_c hd/\hbar^2$ is the KP barrier strength, and the last column compares the analytic and plane-wave $e1$ edge at $k_z = 0$ (measured from the dot CB edge).**

| Design | $h$ $(nm)$ | $d$ $(nm)$ | $E_{IB}^{ctr}$ $(eV)$ | $W_{IB}$ $(meV)$ | $n_b$ | $n_h$ | $W_{hh}$ $(meV)$ | $l_e$ $(nm)$ | $P_{KP}$ | $E_{e2}^{bot}$ $(eV)$ | $E_{e1}(0)$ $(eV)$ |
|---|---|---|---|---|---|---|---|---|---|---|---|
| A | 3 | 6 | 1.699 | 2.95 | 1 | 2 | 0.013 | 1.24 | 9.44 | 1.966 | 0.15123 |
| B | 4 | 4 | 1.649 | 7.63 | 2 | 3 | 0.039 | 1.13 | 8.59 | 1.903 | 0.10827 |
| C | 5 | 2.5 | 1.613 | 17.78 | 3 | 4 | 0.161 | 1.07 | 6.87 | 1.814 | 0.07667 |

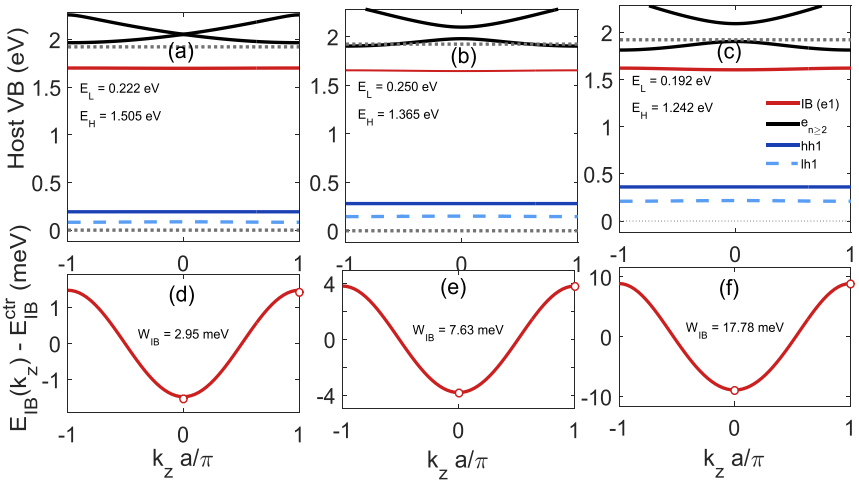



Figure 5: Kronig-Penney minibands of Designs A, B and C. (a)–(c) IB (e1, red), CB-like electron minibands (black), hh1 (blue) and lh1 (dashed light blue), measured from the host VB edge. Dotted lines mark the host band edges. (d)–(f) The IB on a meV scale. Lines: plane-wave solution. Circles: analytic band edges from Eq. (10).

Figure 6 shows the envelope densities at $k_z = 0$. The e1, hh1 and lh1 states are all centred in the dot, so the electron-hole overlaps that govern the VB→IB absorption are large. The light electron mass gives $e1$ an evanescent tail of 1.07-1.24 nm into the spacer, while hh1 is almost fully confined. The $e2$ state has a node at the dot centre and opposite parity to $e1$, which is why the $e1 \rightarrow e2$ coupling is polarisedalong $z$. In Design C the electron density between dots remains at about 10% of its peak, a direct picture of the inter-dot coupling.

Table 7 quantifies the localization as the fraction of each probability density that lies inside the InPBi dot, along the growth axis at $k_z = 0$ and laterally within the radius $R$. Laterally every state is at least 98.6% inside the dot, so the axial fraction is effectively the three dimensional one. The IB electron is 80, 87 and 91% inside the dot in Designs A, B and C, and its remaining weight is the evanescent tail that couples neighbouring dots into the miniband. The heavy hole is 95-99% inside the dot. These values confirm the type-I character of the architecture. The light hole is localized only when Bi deepens its well. At 1% Bi only 46% of lh1 lies in the dot, and the fraction rises to 73 and 86% at 2 and 3% Bi. The second electron level is extended in Design A, where it lies above the barrier and only 8% of it is in the dot, but it becomes a bound dot state in Designs B and C (65 and 85%). The localization of lh1 and $e2$ therefore controls the light-hole and intraband optical transitions which future work shall analyze.

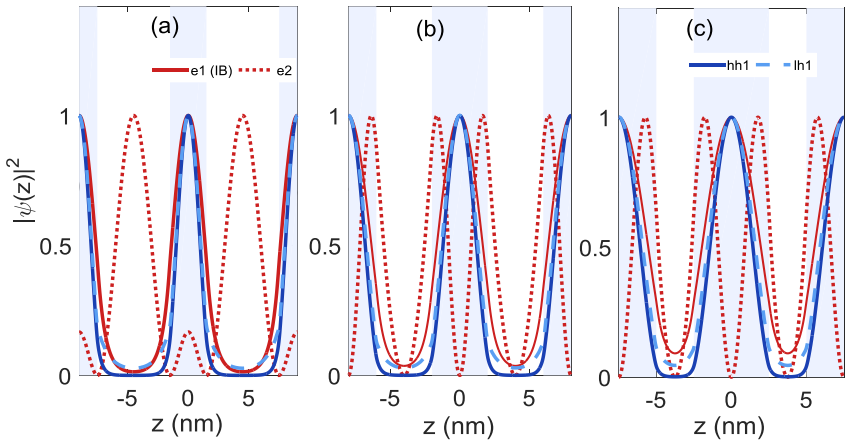



Figure 6: Squared envelopes at $k_z = 0$ for Designs A, B and C over two periods. Red solid: $e1$ (IB). Red dotted: $e2$. Blue: hh1. Dashed light blue: lh1. Shaded regions: InPBi dot layers. The titles give the electron decay length $l_e$ in the spacer.

**Table 7: Probability inside the InPBi dot. Axial fractions are evaluated at $k_z = 0$ over one period; lateral fractions are the probability within the dot radius $R = 10\ nm$.**

| Design | Axial, inside $\|z\| < h/2$ | | | Lateral, inside $\rho < R$ | | | |
|---|---|---|---|---|---|---|---|
| | $e1$(IB) | hh1 | lh1 | $e2$ | $e$ | Hh | lh |
| A | 0.803 | 0.952 | 0.460 | 0.079 | 0.994 | 0.995 | 0.986 |
| B | 0.874 | 0.983 | 0.727 | 0.654 | 0.994 | 0.997 | 0.995 |
| C | 0.908 | 0.992 | 0.861 | 0.854 | 0.995 | 0.998 | 0.997 |

Figure 7 shows how the spacer thickness controls the miniband. For each design geometry, $W_{IB}$ decreases exponentially with $d$, with a decay set by $l_e \approx 1.1 - 1.2\ nm$. For the geometry of Design B it falls from 45 meV at $d$ = 2 nm to 7.6 meV at 4 nm, 1.3 meV at 6 nm and 0.04 meV at 10 nm. A miniband wider than the thermal energy (26 meV) requires $d \leq 2 - 3\ nm$, depending on the dot height. Because the inhomogeneous broadening of SK ensembles is typically 20-30 meV, coherent miniband transport will in practice require such thin spacers, which also favour vertical alignment (Solomon *et al*., 1996; Bimberg *et al*., 1999; Oshima et *al*., 2008; Cuadra *et al*., 2026). The spacer also controls the low gap, as panel (b) shows. $E_L$ rises with $d$ as the miniband narrows and its top moves down, and approaches its isolated-dot value for $d \gtrsim 6 - 8\ nm$. Thin spacers therefore trade voltage for coupling.

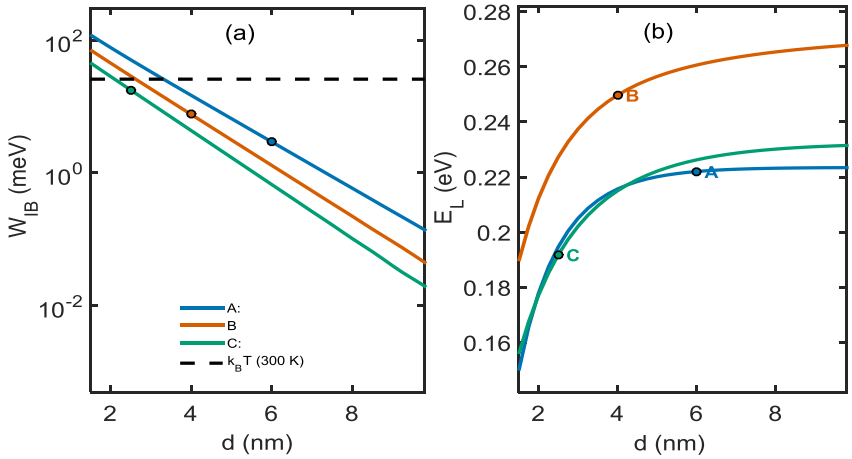



Figure 7: (a) IB width versus spacer thickness for the dot height and Bi fraction of each design (log scale), compared with $K_{BT}$ at 300 K. (b) Low IBSC gap $E_L$ versus spacer thickness. Symbols mark Designs A, B and C.

Figure 8 gives two design maps, and Table 8 summarises the IB gaps. Over $2.5 \leq h \leq 6\ nm$ and $2 \leq d \leq 10\ nm$ at 2% Bi, $E_L$ ranges from 0.14 to 0.27 eV. Its maximum lies near $h \approx 3.75 - 4\ nm$, where the dot is tall enough to deepen the IB but not yet tall enough to bind $e2$. Taller dots bind $e2$ below the host edge and reduce $E_L$ through the confined ladder effect. This is why Design C, despite its strong miniband, has the smallest $E_L$ (0.192 eV). Over $0 \leq x \leq 4\%$ at $d = 4\ nm$, the effective gap $E_g^*$ ranges from 1.33 to 1.81 eV and falls both with dot height and with Bi content. The Bi-induced rise of the hole levels is therefore paid for in $E_g^*$, which sets the voltage of an IBSC. This valence band offset penalty, favours low Bi content. The low gaps $E_L = 0.19 - 0.25\ eV$ are well below the ideal value of about 0.7 eV for a 1.9 eV host (Luque and Marti 1997; Okada *et al*., 2015). This limitation is shared by InAs/GaAs dots (Antolin *et al*., 2010; Ramiro *et al*., 2020) and arises from the 0.40-0.42 eV electron offset.

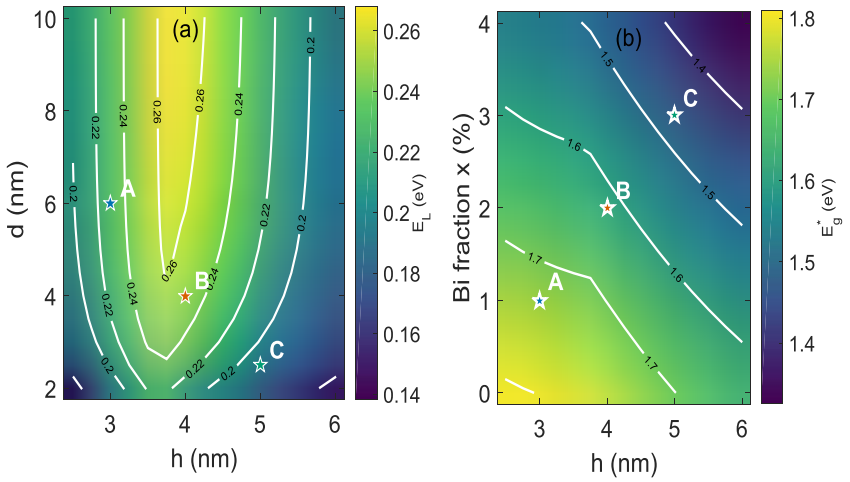



Figure 8: Design maps. (a) $E_L$ over dot height and spacer thickness at 2% Bi. (b) Effective gap $E_g^*$ over dot height and Bi fraction at $d = 4\,nm$. White lines are contours (eV). Stars mark the $(h, d)$ and $(h, x)$ coordinates of Designs A, B and C; in (a) their Bi fractions differ from 2%, which changes $E_L$ by less than 10 meV.

**Table 8: Computed intermediate-band gaps (in eV) of the designs; $\Delta E_{HL}$ is the splitting between the hh1 and lh1 tops.**

| Design | $E_C^*$ | $E_L$ | $E_H$ | $W_{IB}$ | $E_g^*$ | $\Delta E_{HL}$ |
|---|---|---|---|---|---|---|
| A | 1.923 | 0.222 | 1.505 | 0.003 | 1.730 | 0.175 |
| B | 1.903 | 0.250 | 1.365 | 0.008 | 1.623 | 0.208 |
| C | 1.814 | 0.192 | 1.242 | 0.018 | 1.452 | 0.218 |

Bismuth may modify the electron mass of the dot. Figure 9 varies $m_{e,dot}^*$ from 0.06 to $0.12m_0$ with all other parameters fixed. The IB width changes by a factor of only 1.7-2.0, because tunneling is controlled mainly by the host mass and the barrier height, and the IB centre shifts by 24-25 meV. These shifts bound the uncertainty due to the electron mass and are smaller than the inhomogeneous broadening of real ensembles. Uncertainties in $\zeta$ and in the Bi shifts move the offsets by a few tens of meV, which changes the numerical values of $E_L$ and $E_H$ but not the conclusions about host selection, strain balance or miniband formation.

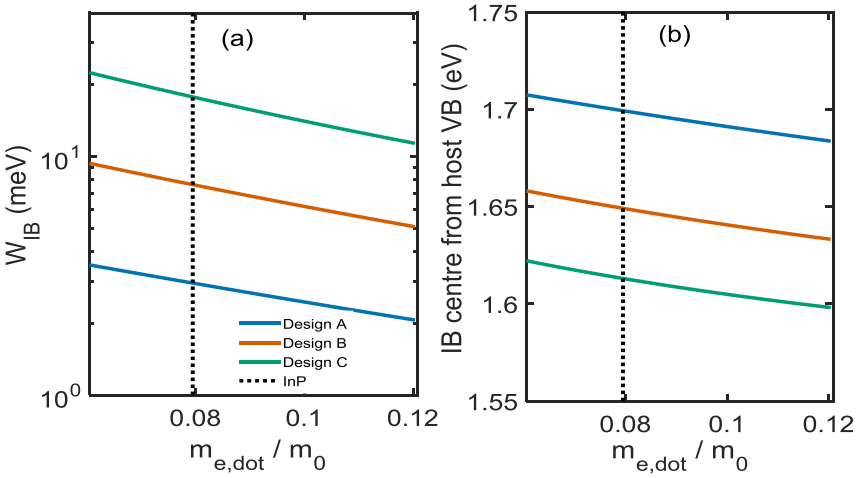



Figure 9: Sensitivity of (a) the IB width and (b) the IB centre to the dot electron mass, for Designs A, B and C. The dotted line marks the InP value.

So far, the intermediate band has been characterised by its position and width. Four further properties decide how it behaves in a solar cell: its response to the Bi content, its effective mass and group velocity along the stack, its density of states in a real ensemble, and the doping needed to fill it. Figure 10 and Table 9summarise them. They follow from the same Kronig-Penney dispersion, $E_{IB}(k_z)$, through

$$\frac{1}{m^*_{IB}} = \frac{1}{\hbar^2}\frac{\delta^2 E_{IB}}{\partial k_z^2},\ v_z(k_z) = \frac{1}{\hbar}\frac{\partial E_{IB}}{\partial k_z},\quad g(E) \propto \sum_{k_z} \delta(E - E_{IB}(k_z) \qquad (16)$$

with the density of states $g(E)$ normalised to one state and, for the ensemble, convolved with the 25 meV Gaussian size distribution (Bimberg *et al*., 1999).

The IB is almost insensitive to bismuth. Over $0 \le x \le 4\%$ its centre moves down by only 7.8-8.9 meV per percent Bi, while the hh1 level rises by 70-72 meV per percent Fig. 10(a). The small IB shift comes from the 13 meV per percent CB shift, partly offset by confinement.

Across the same range $E_L$ changes by at most 32 meV (from 0.214 to 0.246 eV in the geometry of Design A, 0.240 to 0.259 eV in B and 0.183 to 0.195 eV in C), and the IB width changes by less than 2 meV. Bi content can therefore be used to tune the VB side of the device without disturbing the IB.

Along the stack the IB carriers are heavy. At the zone centre the miniband mass is 0.661, 0.337 and 0.181 $m_0$ for Designs A, B and C, which is 8.3, 4.2 and 2.3 times the bulk InP mass. Near the zone edge the curvature reverses and the mass becomes negative (−0.615, −0.288 and −0.126 $m_0$). The mass grows exponentially with spacer thickness Fig. 10(b), from 0.11-0.14 $m_0$ at $d$ = 2 nm to 8-42 $m_0$ at $d$ = 10 nm, so a thick spacer turns the IB into a set of nearly immobile dot states. The maximum group velocity is 2.0, 4.6 and $10.1 \times 10^4 ms^{-1}$ Fig. 10(c), and the time $h/W_{IB}$ for an electron to move between neighbouring dots is 1.4, 0.54 and 0.23 ps. These times are shorter than typical intraband relaxation and recombination times in dot stacks, (Tomi, 2010; Kronig and Penny, 1931) so in an ideal superlattice the IB electrons would be shared between dots before they recombine.

Size fluctuations change this picture. A perfectly periodic stack has a one-dimensional miniband density of states confined within WIB, with van Hove peaks at its edges Fig. 10(d), thin lines. A real ensemble with $\sigma = 25\ meV$ spreads every design into the same Gaussianband of about 60 meV full width (thick lines), because $W_{IB}/2\sigma$ is only 0.06, 0.15 and 0.36. The coherent miniband is then hidden inside the inhomogeneous line, and transport along the stackproceeds by hopping between dots of different size rather than by band conduction (Oshima *et al*., 2008; Cuadra *et al*., 2026). A miniband as wide as $2\sigma = 50\ meV$ would require spacers of about 2.5 nm in the geometry of Design A, 1.9 nm in B and less than 1.5 nm in C. For the present designs the IB is thereforebest described as a narrow, inhomogeneously broadened band of tunnel-coupled dot states.This is the regime of existing InAs/GaAs QD IBSCs, (Okada *et al*., 2015; Antolin *et al*., 2010; Tomic, 2010) and it is the regime assumedfor the absorption calculations projected for future work.

Finally, the IB must be partly filled so that it can both accept electrons from the VB and supply them to the CB (Luque and Marti, 1997; Marti *et al*., 2001). Each dot provides one $s-$like lateral level, or two states including spin, so half-filling requires one electron per dot. For $\sigma_{QD} = 5 \times 10^{10} cm^{-2}$ this is a sheet donor density of $5 \times 10^{10} cm^{-2}$ per dot layer, equivalent to 5.6, 6.3 and $6.7 \times 10^{16} cm^{-3}$ averaged over the period of Designs A, B and C. Silicon $\delta-$doping in the spacer is the standard way to supply it (Marti *et al*.,2001; Antolin *et al*.,2010). In $Al_{0.40}Ga_{0.60}As$, however, silicon forms DX centres that trap the donor electrons (Mooney, 1990), so the $\delta-$layer should be placed in a thin GaAs or low-Al layer next to each dot layer.

**Table 9: Intermediate-band properties (computed). $m^*_{IB}$ is the miniband mass along $z$ at the zone centre and edge, $v_{max}$ the maximum group velocity, $h/W_{IB}$ the inter-dot transfer time, $\sigma = 25\ meV$ the inhomogeneous broadening, and $N_{1/2}$ the donor density for half filling (one electron per dot). The last two columns give the shifts of the IB centre and of the hh1 top per percent Bi.**

| Design | $W_{IB}(me$ | $m^*_{IB}(0)(n$ | $m^*_{IB}(\pi/a)($ | $v_{max}(10^4$ /$s)$ | $h/W_{IB}$ (p | $W_{IB}/2$ | $N_{1/2}(10^{16}cn$ | $dE_{IB}/dx$ (m | $dE_{hh1}/dx$ (n |
|---|---|---|---|---|---|---|---|---|---|
| A | 2.95 | 0.661 | -0.615 | 2.0 | 1.40 | 0.06 | 5.6 | -7.8 | 70.0 |
| B | 7.63 | 0.337 | -0.288 | 4.6 | 0.54 | 0.15 | 6.3 | -8.5 | 71.4 |
| C | 17.78 | 0.181 | -0.126 | 10.1 | 0.23 | 0.36 | 6.7 | -8.9 | 71.9 |

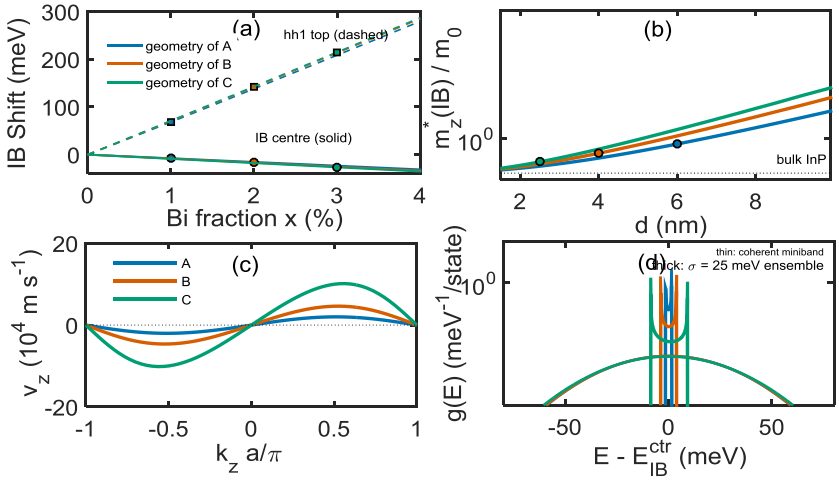



Figure 10: Intermediate band properties. (a) Shift of the IB centre (solid) and of the hh1 top (dashed) with Bi fraction, at the geometry of each design. (b) IB effective mass along z at the zone centre versus spacer thickness; the dotted line marks bulk InP. (c) IB group velocity across the mini-zone. (d) IB density of states per state: thin lines, coherent miniband; thick lines, ensemble with 25 meV Gaussian broadening. Symbols mark Designs A, B and C.

## CONCLUSION

This study presents a theoretical assessment of InPBi/AlGaAs quantum-dot superlattices (QDSLs) for intermediate-band solar cell applications by integrating band alignment, strain compensation, carrier confinement, and Kronig–Penney miniband formation within a common design framework. The main contribution is the identification of a constrained design space in which Bi composition, dot height, spacer thickness, and strain compensation can be considered simultaneously rather than as independent material parameters.

Within the assumptions of the adopted model, InPBi/AlGaAs is predicted to exhibit type-I confinement for electrons, heavy holes, and light holes over the investigated 1–3% Bi range. The calculated conduction and heavy-hole offsets are 0.40–0.42 eV and 0.25–0.40 eV, respectively. Strain coupling to the split-off band is predicted to stabilize the light-hole state and give it predominantly in-plane character. The calculations also predict strong carrier localization, with 80–91% of the IB-electron probability, 95–99% of the heavy-hole probability, and 83–95% of the light-hole probability confined within the dots.

The predicted lowest intermediate band is relatively insensitive to Bi composition, changing by less than 9 meV per percent Bi, while its calculated miniband width is 3–18 meV. These widths are below the assumed 25 meV inhomogeneous broadening, suggesting that practical structures may behave as ensembles of tunnel-coupled dot states rather than ideal narrow minibands. The design maps indicate that dot heights near 4 nm and spacer thicknesses of approximately 2–3 nm or less favour miniband formation. GaP sheets of 0.55–0.78 nm per period are predicted to compensate the approximately 4% compressive strain while remaining below the assumed critical thickness.

The principal new outcome is therefore the combined prediction of electronic confinement, strain compensation, and tunable miniband formation for InPBi/AlGaAs QDSLs, providing specific design targets for future device studies. The predictions are supported by agreement between the Kronig–Penney and plane-wave calculations to approximately 0.05 meV, but this verifies the numerical implementation rather than the experimental material parameters.

The model does not explicitly account for alloy disorder, local strain fluctuations, interface roughness, or Bi segregation and partitioning. These limitations may modify the predicted band offsets, localization, and miniband coupling. Experimental measurements of in-dot strain and InPBi/AlGaAs band offsets, together with atomistic or multiscale calculations incorporating disorder and local strain, are therefore required to test and refine the present predictions..

## REFERENCES

Akahane, K., Matsumoto, A., Umezawa, T., Tominaga, Y. and Yamamoto, N. (2022). Growth of InPBi on InP(311)B substrate by molecular beam epitaxy. *Physica Status Solidi A: Applications and Materials Science, 219*, 2100411. https://doi.org/10.1002/pssa.202100411

Alberi, K., Wu, J., Walukiewicz, W., Yu, K. M., Dubon, O. D., Watkins, S. P., Wang, C. X., Liu, X., Cho, Y. J. and Furdyna, J. (2007). Valence-band anticrossing in

mismatched III–V semiconductor alloys. *Physical Review B, 75*, 045203. https://doi.org/10.1103/PhysRevB.75.045203

Almosni, S., Delamarre, A., Jehl, Z., Suchet, D., Giteau, M., Denis, R., Ory, D., Roman, L., Han, M., Van de Walle, C. G., Delerue, C. and Guillemoles, J.-F. (2018). Material challenges for solar cells in the twenty-first century: Directions in emerging technologies. *Science and Technology of Advanced Materials, 19*, 336–352. https://doi.org/10.1080/14686996.2018.1433439

Antolín, E., Martí, A., Linares, P. G., Ramiro, I., Hernández, E., Farmer, C. D., Stanley, C. R. and Luque, A. (2010). Reducing carrier escape in the InAs/GaAs quantum dot intermediate band solar cell. *Journal of Applied Physics, 108*, 064513. https://doi.org/10.1063/1.3468520

Aspnes, D. E. (1976). GaAs lower conduction-band minima: Ordering and properties. *Physical Review B, 14*, 5331–5343. https://doi.org/10.1103/PhysRevB.14.5331

Bailey, C. G., Forbes, D. V., Raffaelle, R. P. and Hubbard, S. M. (2011). Near 1 V open circuit voltage InAs/GaAs quantum dot solar cells. *Applied Physics Letters, 98*, 163105. https://doi.org/10.1063/1.3580765

Bastard, G. (1981). Superlattice band structure in the envelope-function approximation. *Physical Review B, 24*, 5693–5698. https://doi.org/10.1103/PhysRevB.24.5693

BenDaniel, D. J. and Duke, C. B. (1966). Space-charge effects on electron tunneling. *Physical Review, 152*, 683–692. https://doi.org/10.1103/PhysRev.152.683

Bimberg, D., Grundmann, M. and Ledentsov, N. N. (1999). *Quantum dot heterostructures*. Wiley.

Broderick, C. A., Usman, M., Sweeney, S. J. and O'Reilly, E. P. (2012). Band engineering in dilute nitride and bismide semiconductor lasers. *Semiconductor Science and Technology, 27*, 094011. https://doi.org/10.1088/0268-1242/27/9/094011

Chen, X., Wu, X., Yue, L., Zhu, L., Pan, W., Qi, Z., Wang, S. and Shao, J. (2017). Negative thermal quenching of below-bandgap photoluminescence in InPBi. *Applied Physics Letters, 110*, 051903. https://doi.org/10.1063/1.4975586

Chuang, S. L. (1991). Efficient band-structure calculations of strained quantum wells. *Physical Review B, 43*, 9649–9661. https://doi.org/10.1103/PhysRevB.43.9649

Chuang, S. L. (2009). *Physics of photonic devices* (2nd ed.). Wiley.

Cuadra, L., Perez-Aracil, J. and Salcedo-Sanz, S. (2026). Degradation of the intermediate band caused by disorder in quantum-dot intermediate-band solar cells. *Micromachines, 17*, 1005. https://doi.org/10.3390/mi17091005

Ekins-Daukes, N. J., Kawaguchi, K. and Zhang, J. (2002). Strain-balanced criteria for multiple quantum well structures and its signature in X-ray rocking curves. *Crystal Growth & Design, 2*, 287–292. https://doi.org/10.1021/cg025502y

Grundmann, M., Stier, O. and Bimberg, D. (1995). InAs/GaAs pyramidal quantum dots: Strain distribution, optical phonons, and electronic structure. *Physical Review B, 52*, 11969–11981. https://doi.org/10.1103/PhysRevB.52.11969

Gu, Y., Wang, K., Zhou, H., Li, Y., Cao, C., Zhang, L., Zhang, Y., Gong, Q. and Wang, S. (2014). Structural and optical characterizations of InPBi thin films grown by molecular beam epitaxy. *Nanoscale Research Letters, 9*, 24. https://doi.org/10.1186/1556-276X-9-24

Hahn, R. V. H., Califano, M., Rodríguez-Bolívar, S. and Gómez-Campos, F. M. (2025). Coupled 2D quantum dot films for next generation solar cells: Electronic structure and anomalous light absorption behaviour. *Nanoscale, 17*, 10732–10742. https://doi.org/10.1039/D4NR04841E

Harrison, P. and Valavanis, A. (2016). *Quantum wells, wires and dots* (4th ed.). Wiley.

Hatami, F. (2003). InP quantum dots embedded in GaP: Optical properties and carrier dynamics. *Physical Review B, 67*, 085306. https://doi.org/10.1103/PhysRevB.67.085306

Hubbard, S. M., Cress, C. D., Bailey, C. G., Raffaelle, R. P., Bailey, S. G. and Wilt, D. M. (2008). Effect of strain compensation on quantum dot enhanced GaAs solar cells. *Applied Physics Letters, 92*, 123512. https://doi.org/10.1063/1.2894527

Kim, K., Hart, G. L. W. and Zunger, A. (2002). Negative band gap bowing in epitaxial InAs/GaAs alloys and predicted band offsets of the strained binaries and alloys on various substrates. *Applied Physics Letters, 80*, 3105–3107. https://doi.org/10.1063/1.1470693

Kopaczek, J., Kudrawiec, R., Polak, M. P., Scharoch, P., Birkett, M., Veal, T. D., Wang, K., Gu, Y., Gong, Q. and Wang, S. (2014). Contactless electroreflectance and theoretical studies of band gap and spin-orbit splitting in $InP_{1-x}Bi_x$ dilute bismide with $x \leq 0.034$. *Applied Physics Letters*, *105*, 222104. https://doi.org/10.1063/1.4903179

Kronig, R. de L. and Penney, W. G. (1931). Quantum mechanics of electrons in crystal lattices. *Proceedings of the Royal Society of London. Series A*, *130*, 499–513. https://doi.org/10.1098/rspa.1931.0019

Lazarenkova, O. L. and Balandin, A. A. (2001). Miniband formation in a quantum dot crystal. *Journal of Applied Physics*, *89*, 5509–5518. https://doi.org/10.1063/1.1366662

Leonard, D., Krishnamurthy, M., Reaves, C. M., DenBaars, S. P. and Petroff, P. M. (1993). Direct formation of quantum-sized dots from uniform coherent islands of InGaAs on GaAs surfaces. *Applied Physics Letters*, *63*, 3203–3205. https://doi.org/10.1063/1.111587

Luque, A. and Martí, A. (1997). Increasing the efficiency of ideal solar cells by photon induced transitions at intermediate levels. *Physical Review Letters*, *78*, 5014–5017. https://doi.org/10.1103/PhysRevLett.78.5014

Luque, A. and Martí, A. (2010). The intermediate band solar cell: Progress toward the realization of an attractive concept. *Advanced Materials*, *22*, 160–174. https://doi.org/10.1002/adma.200902388

Luque, A., Martí, A. and Stanley, C. (2012). Understanding intermediate-band solar cells. *Nature Photonics*, *6*, 146–152. https://doi.org/10.1038/nphoton.2012.1

Luque, A., Martí, A., Antolín, E., Linares, P. G., Tobias, I. and Ramiro, I. (2012). Understanding the operation of quantum dot intermediate band solar cells. *Journal of Applied Physics*, *111*, 044502. https://doi.org/10.1063/1.3693181

Luttinger, J. M. (1956). Quantum theory of cyclotron resonance in semiconductors: General theory. *Physical Review*, *102*, 1030–1041. https://doi.org/10.1103/PhysRev.102.1030

Martí, A., Antolín, E., Stanley, C. R., Farmer, C. D., López, N., Díaz, P., Cánovas, E., Linares, P. G. and Luque, A. (2006). Production of photocurrent due to intermediate-to-conduction-band transitions: A demonstration of a key operating principle of the intermediate-band solar cell. *Physical Review Letters*, *97*, 247701. https://doi.org/10.1103/PhysRevLett.97.247701

Martí, A., Cuadra, L. and Luque, A. (2001). Partial filling of a quantum dot intermediate band for solar cells. *IEEE Transactions on Electron Devices*, *48*, 2394–2399. https://doi.org/10.1109/16.954482

Matthews, J. W. and Blakeslee, A. E. (1974). Defects in epitaxial multilayers: I. Misfit dislocations. *Journal of Crystal Growth*, *27*, 118–125. https://doi.org/10.1016/S0022-0248(74)80055-2

Mooney, P. M. (1990). Deep donor levels (DX centers) in III–V semiconductors. *Journal of Applied Physics*, *67*, R1–R18. https://doi.org/10.1063/1.345628

Neupane, K., Kabel, J., Uddin, J., Dubey, R., Ojha, R., Zhang, D. and Yap, Y. K. (2026). Quantum dot solar cells: Background, progress, and perspective. *Micromachines*, *17*, 474. https://doi.org/10.3390/mi17040474

Okada, Y., Ekins-Daukes, N. J., Kita, T., Tamaki, R., Yoshida, M., Pusch, A., Hess, O., Phillips, C. C., Farrell, D. J., Yoshida, K., Ahsan, N., Shoji, Y., Sogabe, T. and Guillemoles, J.-F. (2015). Intermediate band solar cells: Recent progress and future directions. *Applied Physics Reviews*, *2*, 021302. https://doi.org/10.1063/1.4916561

Oshima, R., Takata, A. and Okada, Y. (2008). Strain-compensated InAs/GaNAs quantum dots for use in high-efficiency solar cells. *Applied Physics Letters*, *93*, 083111. https://doi.org/10.1063/1.2973398

Pan, W., Wang, P., Wu, X., Wang, K., Cui, J., Yue, L., Zhang, L., Gong, Q. and Wang, S. (2016). Growth and material properties of InPBi thin films using gas source molecular beam epitaxy. *Journal of Alloys and Compounds*, *656*, 777–782. https://doi.org/10.1016/j.jallcom.2015.10.024

Polak, M. P., Scharoch, P. and Kudrawiec, R. (2015). First-principles calculations of bismuth induced changes in the band structure of dilute Ga–V–Bi and In–V–Bi alloys: Chemical trends versus experimental data. *Semiconductor Science and Technology*, *30*, 094001. https://doi.org/10.1088/0268-1242/30/9/094001

Popescu, V., Bester, G., Hanna, M. C., Norman, A. G. and Zunger, A. (2008). Theoretical and experimental examination of the intermediate-band concept for strain-balanced (In,Ga)As/Ga(As,P) quantum dot solar cells.

*Physical Review B, 78*, 205321. https://doi.org/10.1103/PhysRevB.78.205321

Pryor, C. E. and Pistol, M. E. (2005). Band-edge diagrams for strained III–V semiconductor quantum wells, wires, and dots. *Physical Review B, 72*, 205311. https://doi.org/10.1103/PhysRevB.72.205311

Ramiro, I. and Martí, A. (2021). Intermediate band solar cells: Present and future. *Progress in Photovoltaics: Research and Applications, 29*, 705–716. https://doi.org/10.1002/pip.3351

Ramiro, I., Villa, J., Hwang, J., Martin, A. J., Millunchick, J., Phillips, J. and Martí, A. (2020). Demonstration of a GaSb/GaAs quantum dot intermediate band solar cell operating at maximum power point. *Physical Review Letters, 125*, 247703. https://doi.org/10.1103/PhysRevLett.125.247703

Shalindar, A. J., Webster, P. T., Wilkens, B. J., Alford, T. L. and Johnson, S. R. (2016). Measurement of InAsBi mole fraction and InBi lattice constant using Rutherford backscattering spectrometry and X-ray diffraction. *Journal of Applied Physics, 120*, 145704. https://doi.org/10.1063/1.4964799

Shockley, W. and Queisser, H. J. (1961). Detailed balance limit of efficiency of p–n junction solar cells. *Journal of Applied Physics, 32*, 510–519. https://doi.org/10.1063/1.1736034

Solomon, G. S., Trezza, J. A., Marshall, A. F. and Harris, J. S. (1996). Vertically aligned and electronically coupled growth induced InAs islands in GaAs. *Physical Review Letters, 76*, 952–955. https://doi.org/10.1103/PhysRevLett.76.952

Stier, O., Grundmann, M. and Bimberg, D. (1999). Electronic and optical properties of strained quantum dots modeled by 8-band k·p theory. *Physical Review B, 59*, 5688–5701. https://doi.org/10.1103/PhysRevB.59.5688

Sugaya, T., Furue, Y., Komaki, H., Amano, T., Mori, M., Komori, K., Niki, S., Numakami, O. and Okano, Y. (2012). Ultra-high stacks of InGaAs/GaAs quantum dots for high efficiency solar cells. *Energy & Environmental Science, 5*, 6233–6237. https://doi.org/10.1039/C2EE01930B

Tersoff, J., Teichert, C. and Lagally, M. G. (1996). Self-organization in growth of quantum dot superlattices. *Physical Review Letters, 76*, 1675–1678. https://doi.org/10.1103/PhysRevLett.76.1675

Tomić, S. (2010). Intermediate-band solar cells: Influence of band formation on dynamical processes in InAs/GaAs quantum dot arrays. *Physical Review B, 82*, 195321. https://doi.org/10.1103/PhysRevB.82.195321

Tomić, S., Jones, T. S. and Harrison, N. M. (2008). Absorption characteristics of a quantum dot array induced intermediate band: Implications for solar cell design. *Applied Physics Letters, 93*, 263105. https://doi.org/10.1063/1.3058716

Tomić, S., Martí, A., Antolín, E. and Luque, A. (2011). On inhibiting Auger intraband relaxation in InAs/GaAs quantum dot intermediate band solar cells. *Applied Physics Letters, 99*, 053504. https://doi.org/10.1063/1.3621876

Van de Walle, C. G. (1989). Band lineups and deformation potentials in the model-solid theory. *Physical Review B, 39*, 1871–1883. https://doi.org/10.1103/PhysRevB.39.1871

Vullum, P. E., Nord, M., Vatanparast, M., Thomassen, S. F., Boothroyd, C., Holmestad, R., Fimland, B. O. and Reenaas, T. W. (2017). Quantitative strain analysis of InAs/GaAs quantum dot materials. *Scientific Reports, 7*, 45376. https://doi.org/10.1038/srep45376

Vurgaftman, I., Meyer, J. R. and Ram-Mohan, L. R. (2001). Band parameters for III–V compound semiconductors and their alloys. *Journal of Applied Physics, 89*, 5815–5875. https://doi.org/10.1063/1.1368156

Wang, K., Gu, Y., Zhou, H. F., Zhang, L. Y., Kang, C. Z., Wu, M. J., Pan, W. W., Lu, P. F., Gong, Q. and Wang, S. (2014). InPBi single crystals grown by molecular beam epitaxy. *Scientific Reports, 4*, 5449. https://doi.org/10.1038/srep05449

Wang, L., Zhang, L., Yue, L., Liang, D., Chen, X., Li, Y., Lu, P., Shao, J. and Wang, S. (2017). Novel dilute bismide, epitaxy, physical properties and device application. *Crystals, 7*, 63. https://doi.org/10.3390/cryst7030063

Wang, S. and Lu, P. (Eds.). (2019). *Bismuth-containing alloys and nanostructures* (Springer Series in Materials Science, Vol. 285). Springer. https://doi.org/10.1007/978-3-030-15036-6

Wu, X., Chen, X., Pan, W., Wang, P., Zhang, L., Li, Y., Wang, H., Wang, K., Shao, J. and Wang, S. (2016). Anomalous photoluminescence in $InP_{1-x}Bi_x$. *Scientific Reports, 6*, 27867. https://doi.org/10.1038/srep27867

Xie, Q., Madhukar, A., Chen, P. and Kobayashi, N. P. (1995). Vertically self-organized InAs quantum box islands on GaAs(100). *Physical Review Letters*, *75*, 2542–2545. https://doi.org/10.1103/PhysRevLett.75.2542

Zhang, L., Song, Y. and Gong, Q. (2019). GaAs-based InPBi quantum dots for high efficiency super-luminescence diodes. *International Journal of Molecular Sciences*, *20*, 6001. https://doi.org/10.3390/ijms20236001

Zhang, L., Song, Y., Chen, Q., Zhu, Z. and Wang, S. (2018). InPBi quantum dots for superluminescence diodes. *Nanomaterials*, *8*, 705. https://doi.org/10.3390/nano8090705

Zhang, L., Wu, M., Chen, X., Wu, X., Spiecker, E., Song, Y., Pan, W., Li, Y., Yue, L., Shao, J. and Wang, S. (2017). Nanoscale distribution of Bi atoms in $InP_{1-x}Bi_x$. *Scientific Reports*, *7*, 12278. https://doi.org/10.1038/s41598-017-12075-2